PHYSICAL REVIEW B **92**, 054433 (2015)

Correlations between structural, electronic transport, and magnetic properties of $Co_2FeAl_{0.5}Si_{0.5}$ Heusler alloy epitaxial thin films

M. S. Gabor,[1,*] M. Belmeguenai,[2] T. Petrisor, Jr.,[1] C. Ulhaq-Bouillet,[3] S. Colis,[3] and C. Tiusan[1,4,†]

[1]*Center for Superconductivity, Spintronics and Surface Science, Physics and Chemistry Department, Technical University of Cluj-Napoca, Str. Memorandumului No. 28 RO-400114 Cluj-Napoca, Romania*

[2]*LSPM (CNRS-UPR 3407) 99 avenue Jean-Baptiste Clément, Université Paris 13, 93430 Villetaneuse, France*

[3]*Institut de Physique et Chimie des Matériaux de Strasbourg (IPCMS), UMR 7504 UDS-CNRS and Université de Strasbourg (UDS-ECPM), 23 rue du Loess, BP43, F-67034 Strasbourg Cedex 2, France*

[4]*Institut Jean Lamour, CNRS, Universite Lorraine, BP 70239, F 54506 Vandoeuvre, France*

(Received 24 February 2015; revised manuscript received 2 July 2015; published 25 August 2015)

The structural and chemical order are the most important parameters governing the physical properties of the Heusler compounds. Here, we give a comprehensive overview of the correlations between structural and chemical order, electronic transport (longitudinal and transverse) and magnetic (static and dynamic) properties of $Co_2FeAl_{0.5}Si_{0.5}$ Heusler alloy epitaxial thin films grown on MgO(001) single-crystal substrates. X-ray diffraction measurements indicated that depending on the annealing temperature the films show $B2$ or $L2_1$ chemical ordering. Longitudinal magnetoresistivity experiments revealed that for the best $L2_1$ ordered film, at temperatures bellow 125 K, the magnon assisted electronic scattering is quenched indicating the appearance of half-metallicity. The presence of quantum correction in resistivity, whose strength is dependent on the structural ordering, was evidenced at low temperatures. Anomalous Hall experiments indicated that the intrinsic band structure contribution has an opposite sign and that is dominant over the extrinsic skew scattering mechanism. The presence of a small uniaxial magnetic anisotropy contribution superimposed on a larger biaxial one was evidenced via ferromagnetic resonance microstrip line measurements. The biaxial term is well correlated with chemical ordering, having a minimum value for the optimum $L2_1$ ordered film. The damping parameter was evaluated from ferromagnetic resonance linewidth measurements, and a coefficient as low as 1.9×10^{-3} was found for the $L2_1$ phase.

DOI: 10.1103/PhysRevB.92.054433 PACS number(s): 85.75.−d, 75.70.Ak, 73.50.Jt, 75.47.Np

I. INTRODUCTION

One of the key parameters in operating the spintronic devices [1] is the spin polarization of the electronic current. The optimization of this parameter often implicates complex studies leading to the development of highly spin-polarized innovative magnetic materials. They should constitute the spin polarizer in complex multilayer stack spintronic architectures. Within this problematic, since they show a band gap at the Fermi level for the minority spins, the half-metallic ferromagnets (HMFs) [2] are considered ideal candidates as spin-polarized electronic current sources. Amongst the different types of HMFs, the Co-based full Heusler alloys are of special importance due their theoretically predicted half-metallicity [3,4] and relatively high Curie temperature [5]. Two of the most important Co-based full Heusler alloys are Co_2FeAl and Co_2FeSi. They are with high Curie temperature and low Gilbert damping [6–9]. Moreover, using Co_2FeAl and Co_2FeSi electrodes, MgO (001) based magnetic tunnel junctions (MTJs) with relatively large magnetoresistive ratios [10,11] have been elaborated. Therefore these two materials show a huge potential for applications in data storage, read-head sensors, or high-frequency spin-torque driven oscillators whose elementary brick is the magnetic tunnel junction.

However, despite the promising theoretical premises, the underlying physics governing the magnetic properties and spin and charge transport mechanisms in ferromagnetic Heusler alloy films remains complex, yet. Moreover, for an optimum integration in spintronic devices, the Heusler alloy films have to simultaneously meet several challenges. Half-metallicity, responsible for the large spin polarization, is required at room temperature and not only at low temperature, where the theoretical calculations often describe the system. Besides the spin polarization, another important physical property of spintronic devices ferromagnetic electrodes is the Gilbert damping. A low damping is essential for spin switching with low currents in spin transfer torque MTJs and spin torque oscillators [12]. However, in the case of the all-metal current perpendicular to plane (CPP) spin valves, a high spin polarization combined with a low Gilbert damping of the ferromagnetic material of the electrodes would lead to important magnetic-noise values through spin-torque effects [13]. Therefore an optimum value of Gilbert damping is required, depending on the class of the final spintronic application.

The macroscopic properties of Heusler alloys are tightly correlated to their electronic structure. Therefore tailoring the electronic structure of the alloy provides a track for material properties optimization. Band-structure calculations [14] have indicated that the Fermi level lays near to the top of the valence or bottom of the conduction bands of minority spins for Co_2FeAl and Co_2FeSi, respectively. This makes the two compounds prone to finite temperature effects detrimental to half-metallicity. An immediate solution to avoid such effects is the alloying of the two compounds to form $Co_2FeAl_{0.5}Si_{0.5}$ (CFAS). The main calculated effect of alloying is the virtual movement of the Fermi level in the middle of the minority

*Corresponding author: mihai.gabor@phys.utcluj.ro
†Corresponding author: coriolan.tiusan@phys.utcluj.ro

 ©2015 American Physical Society

spins gap [14] and thus the improvement of the half-metallicity stability. Indeed, directly correlated to a large spin polarization, relatively large magnetoresistance values were observed in CPP spin valves and MTJs integrating CFAS electrodes [15–18].

In direct correlation with their electronic structure, the spin polarization of full-Heusler alloys depends on the chemical ordering [19]. Moreover, since it has a direct impact on the electronic structure, the chemical ordering is expected to have a strong impact on longitudinal and transverse electronic transport, and furthermore, on the magnetic anisotropy and damping.

Therefore, in this paper, by combining structural, static and dynamic magnetic and magnetotransport complementary techniques, we perform a comprehensive correlated analysis of related physical properties of both CFAS thin films and lithographically patterned microstructures. We point out the interplay between the ordering (crystallographic and chemical), triggered by thermal annealing, and the longitudinal and transverse electronic transport, magnetic anisotropy and damping of CFAS thin films epitaxially grown on MgO (001) single-crystal substrates. The chemical ordering of the CFA films is tuned form $B2$ to $L2_1$, by increasing the annealing temperature. Longitudinal magnetoresistivity experiments revealed that for the best $L2_1$ ordered films, at temperatures below 125 K, the magnon assisted electronic scattering is quenched indicating the appearance of the half-metallic gap. This implicates the attainment of one of our targeted milestones related to the large spin polarization. Analysis of resistivity temperature dependence reveals important spin and charge transport mechanisms in CFAS. Anomalous resistivity dependence at low temperatures in structural disordered CFAS has been correlated with quantum correction effects involving some possible mechanisms such as the weak localization, the electron-electron interactions in the presence of disorder or the orbital Kondo effect. Anomalous Hall experiments for samples with variable degree of order revealed the scattering mechanism responsible for the anomalous Hall effect (AHE) and indicate that the intrinsic band structure contribution is dominant. The extrinsic skew scattering contribution is found to be non-negligible and shows an opposite sign compared to the intrinsic one. Beyond the transport mechanisms, static and dynamic magnetic characterizations of the CFAS films point out the presence of a small uniaxial magnetic anisotropy contribution superimposed on a larger biaxial term, well correlated with chemical ordering. Finally, our comprehensive analysis demonstrates the major impact of the chemical ordering on: (i) the longitudinal magnetotransport, (ii) the spin-polarization driven by the half-metallicity, and (iii) the major dynamic figure of merit of Heusler films related to the low and tunable Gilbert damping. The correlated knowledge of the structural, electronic transport and magnetic properties provided by our complex study represents a prerequisite for the successful integration of CFAS Heusler films in spintronic devices.

II. EXPERIMENTAL

The CFAS films were grown on MgO(001) single-crystal substrates by DC magnetron sputtering in a system having a base pressure better than 1×10^{-8} Torr. Prior to the deposition of the CFAS films, a 5-nm-thick MgO buffer layer was grown at room temperature (RT) by rf sputtering from a MgO polycrystalline target under an Argon pressure of 10 mTorr. Next, the $d = 25$ nm thick CFAS films were sputtered at RT from a stoichiometric target ($Co_{50\%}Fe_{25\%}Al_{12.5\%}Si_{12.5\%}$) under 1.0 mTorr of Ar. Finally, the films were capped with 5 nm of MgO. After growth, the stacks were *ex situ* annealed for 1 hour in a vacuum better than 5×10^{-8} Torr at various temperatures up to 750 °C. The structural properties of the samples have been analyzed by x-ray diffraction (XRD) using a four circles diffractometer. Additional information on the structural properties was obtained by the transmission electron microscopy. The observations were carried out using a JEOL 2100F microscope Cs corrected at the probe level, with a point to point resolution of 0.22 nm.The static magnetic characteristics have been investigated at RT by vibrating sample magnetometry (VSM). The dynamic magnetic measurements were carried out by microstrip line ferromagnetic resonance (MS-FMR) technique using a homemade setup that allows both frequency and field sweeps [7]. For the electronic transport measurements the samples were patterned by UV lithography and Ar ion milling in the form of Hall bars [inset of Fig. 8(a)]. Resistivity and Hall experiments were performed using standard DC techniques in a temperature range between 3 and 300 K and in magnetic fields up to 70 kOe.

III. RESULTS AND DISCUSSIONS

A. Structural properties

Figure 1(a) shows the $2\theta/\omega$ (out-of-plane) x-ray diffraction patterns recorded for the CFAS films as-deposited and annealed at different temperatures. One can observe that, besides the peak corresponding to the MgO substrate, the patterns show only the (002) and (004) CFAS peaks. This indicates the out-of-plane (00l) textured growth of the CFAS layers. In order to confirm the epitaxial growth of the CFAS films on MgO(001) Φ-scan measurements were employed. The inset of Fig. 1(a) shows Φ-scan measurements for the CFAS (022) and MgO (022) type reflections, performed on the 650 °C annealed film. The Φ scans were measured at a tilt angle $\Psi = 45°$. The fourfold symmetry of the (022) CFAS reflections proves that the films are in-plane oriented. Moreover, the $\Phi = 45°$ angle separation between the CFAS (022) and the MgO(022) type reflections indicates the epitaxial relation: CFAS(001)[110]//MgO(001)[100].

In order to have further insight on the crystalline structure of the films, cross section transmission electron microscopy observations were carried out on a 650 °C annealed sample. Figures 2(a) and 2(b) shows the bright field images of the sample indicating that the film is homogeneous, with very limited roughness and thickness fluctuations. The high-resolution image shows clearly the presence of vertical atomic planes running along the whole film thickness, without visible fractures or changes in orientation. The single-crystalline character is also confirmed by the selected area diffraction pattern [Fig. 2 (c)]. The pattern confirms the XRD determined epitaxial relation. The CFAS diffraction spots show a small elliptic character suggesting a reduced mosaicity of the film.

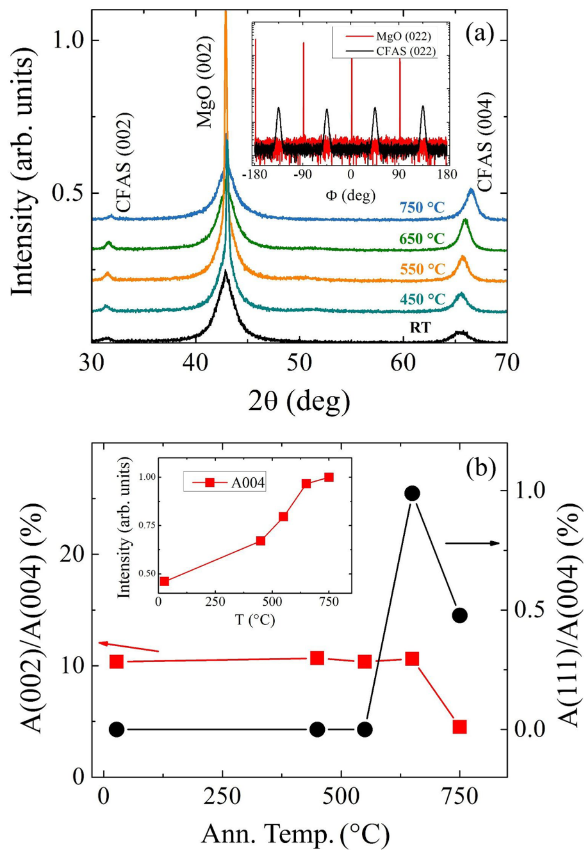

FIG. 1. (Color online) (a) $2\theta/\omega$ (out-of plane) x-ray diffraction patterns for the CFAS films as-deposited and annealed at different temperatures. The inset shows Φ scan measurements around CFAS and MgO (022) type reflections. (b) The A(002)/A(004) and A(111)/A(004) integrated intensity ratios dependence on the annealing temperature. The inset shows the annealing temperature dependence of the normalized integral intensity of the (004) CFAS peak.

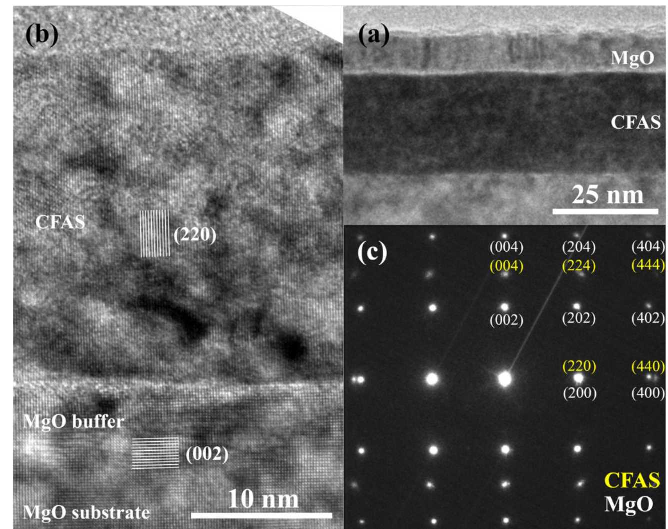

FIG. 2. (Color online) (a) Low- and (b) high-resolution cross section TEM images of the CFAS sample annealed at 650 °C. (c) Selected area electron diffraction patterns showing the MgO and CFAS spots.

This mosaicity, along the film thickness, is coherent with the width of the peaks observed in XRD measurements. The TEM analyses show that along the growth axis, the crystallite size equals the film thickness. The XRD data shows a single-crystal character for all samples and relatively similar full widths at half-maximum (FWHM) of the diffraction peaks for annealed samples. Therefore it can be assumed that crystallites have sizes limited by the film thickness. The as deposited sample shows a rather larger FWHM of the XRD data as compared with the annealed ones. However, we attribute the increased FWHM to the line broadening due to micro-strains induced during the growth process and which are relaxed by annealing [20].

The stoichiometry of the samples has been analyzed by energy dispersive x-ray spectroscopy (EDS) using a transmission electron microscope (TEM) and a scanning electron microscope (SEM). Within the uncertainty limits of the above mentioned techniques we can fairly assume that the stoichiometry of the target is transferred to the films. Moreover, the saturation magnetization of the 650 °C annealed CFAS films is $5.4 \pm 0.1\mu_B$/f.u., value, which is expected for the correct stoichiometry [21].

In terms of chemical order, the CFAS crystal may be in the chemically ordered $L2_1$ phase, the $B2$ phase characterized by disorder between Fe and Al-Si and regular occupation on the Co atomic sites, and the $A2$ phase with random occupation of the Fe, Al-Si, and Co atomic sites. The ordered $L2_1$ structure is characterized by the presence of odd $(h+k+l=2n+1)$ superlattice reflections such as (111) or (311). In contrast, this type of reflections is forbidden in the case of the $B2$ structure, which is characterized by the $h+k+l=4n+2$ superlattice reflections like (002). The $h+k+l=4n$ reflections, like (004) or (224), are fundamental ones corresponding to the cubic lattice and are unaffected by the chemical order [22].

The inset of Fig. 1(b) depicts the annealing temperature dependence of the normalized integral intensity A(004) of the (004) CFAS diffraction peak. The A(004) value shows a monotonic increase with the annealing temperature which implies a constant improvement of the crystal structure of the CFAS films. Since the (004) reflection is a fundamental one and its intensity does not depend on the chemical order, the integrated peak intensity ratio A(002)/A(004) represents a measure of the degree of order on Co sites.

This ratio, shown in Fig. 1(b), has a value roughly independent on the annealing temperature up to 650 °C and consistent with previous reports on high-quality sputter deposited CFAS films [23,24]. For the 750 °C annealed samples, the A(200)/A(400) ratio shows an important decrease. This indicates that the as-deposited films show already B2 ordering and, although we have a monotonous increase of the crystallinity of the films, the B2 ordering does not change up to the 650 °C annealing temperature. The A(111)/A(004) integrated peak intensity ratio represents a measure of the degree $L2_1$ chemical ordering. This ratio, depicted in Fig. 1(b), has a nonzero value only for annealing temperatures higher than 550 °C and shows a maximum for the 650 °C one. Interestingly, for the 750 °C annealing temperature, both the A(002)/A(004) and the A(111)/A(004) show a decrease relatively to the 650 °C

one. This might be an indication of the development of the $DO3$ type disorder [9], i.e., disorder related to the exchange between Co and Fe atomic sites. However, a precise evaluation of the degree of $DO3$ type disorder requires requires special measurement setups such as neutron diffraction, synchrotron XRD, and nuclear magnetic resonance [9,25].

From the above arguments, it can be concluded that the as-deposited and up to 550 °C annealed CFAS films show B2 ordering. For higher annealing temperatures, the films exhibit the $L2_1$ phase, with a maximum degree of $L2_1$ ordering at an annealing temperature of 650 °C. It is to be mentioned that, due to thermodynamic stability reasons, even the best order films most likely show a mixture of $B2$ and $L2_1$ phases [25–27]. As it will be shown in the next sections, the evolution of the ordering is well correlated with the electronic transport, magnetic anisotropy and FMR linewidth.

B. Temperature dependent transport properties

1. *High temperatures $T > 40$ K*

Figure 3 shows the temperature dependence of the longitudinal electrical resistivity ρ_{xx} of the CFAS films as deposited and annealed at different temperatures. All the films show similar trends: a resistivity minimum (ρ_{xx0}) measured at $T_{\rm min} = 15$–30 K, a small upturn in resistivity for lower temperatures and a metalliclike increase of resistivity for higher temperatures. Here, we discuss only the high-temperature behavior ($T > T_{\rm min}$), the low-temperature ($T < T_{\rm min}$) case will be treated in the next section.

It is convenient to describe the resistivity in terms of temperature independent and temperature dependent contributions: $\rho_{xx} = \rho_{xx0} + \rho_{xxT}(T)$. The ρ_{xx0}, which is associated with scattering on structural imperfections, shows a monotonous decrease with increasing annealing temperature (see also inset of Fig. 6) in agrement with the overall improvement of the crystal quality of the films, as evidenced by XRD experiments [inset of Fig. 1(b)]. Moreover, the resistivity ratio (RR) defined as $\rho_{xx}(300\,\text{K})/\rho_{xx0}$ shows an increase with annealing temperature form 1.06 for the as-deposited sample up to 1.18 for the 750 °C annealed one, in accordance with the improvement of the films quality with annealing. Such

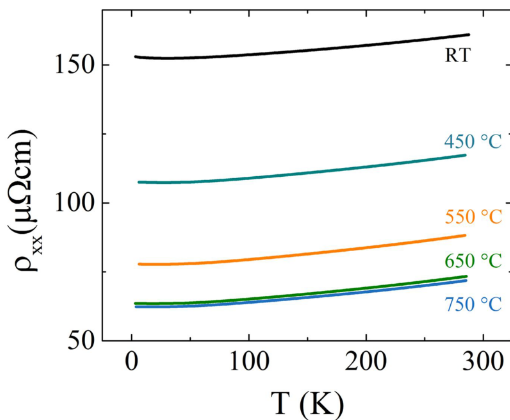

FIG. 3. (Color online) Electrical resistivity as a function of temperature for the CFAS films as deposited and annealed at different temperatures.

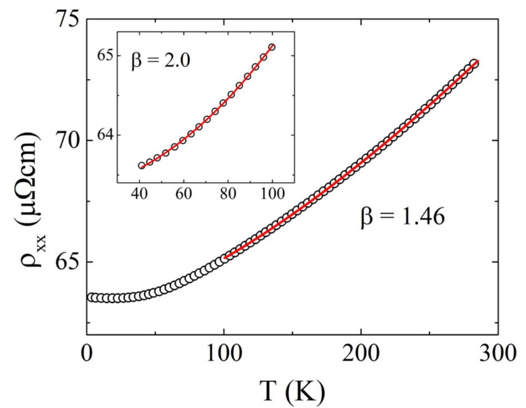

FIG. 4. (Color online) Electrical resistivity as a function of temperature for the CFAS film annealed at 650 °C. The inset shows a zoom in the of the low-temperature region (40 K $< T <$ 100 K). The circles stand for experimental data while the red solid lines represents theoretical fits using the power-law equation.

relative low values of the RR are not uncommon for Heusler alloy thin films [23,28,29] and indicate a relative high degree of temperature independent scattering on crystal imperfections.

In general, for a ferromagnetic film, the temperature dependent part of the resistivity is a result of electron-phonon scattering (ρ^p_{xx}), electron-electron interactions (ρ^e_{xx}), and electron-spin wave scattering (ρ^m_{xx}). According to Matthiessen rule the contributions will add up as:

$$\rho_{xxT}(T) = \rho^p_{xx}(T) + \rho^e_{xx}(T) + \rho^m_{xx}(T). \tag{1}$$

The above scattering terms might show different power-law temperature dependence. Therefore, in order to analyze the temperature dependence of the resistivity of the films, we have fitted our data using the equation:

$$\rho_{xx} = A + BT^{\beta}, \tag{2}$$

where A and B are two real constants. Figure 4 shows the electrical resistivity as a function of temperature for the film annealed at 650 °C and the fit using the power-law equation (2). In the high-temperature region, the data is well fitted using a $\rho_{xx} \propto T^{1.46}$ dependence. All the other films show roughly similar exponents, except for the as deposited film for which the exponent show an increase up to 1.54. Here, the exponent has to be considered as an effective one which accounts for different scattering mechanisms. Similar values of the high-temperature exponent have been previously reported for Heusler alloys [30–32] and, most likely, it is a result of a mixed magnonic and phononic related scattering mechanisms. In the high-temperature region, the phononic component usually leads to a linear temperature dependence. At the same time, the magnonic contribution to the resistivity generally leads to a quadratic temperature dependence in the low-temperature range [33–35]. However, in half-metals, the one-magnon scattering process is forbidden due to the absence of minority spin states at the Fermi level and it is replaced by the two-magnon scattering, which leads to a $T^{4.5}$ and a $T^{3.5}$ dependence at low and high temperatures, respectively [36]. Nonetheless, in half-metals the finite temperature spin fluctuations may induce minority states at the Fermi level,

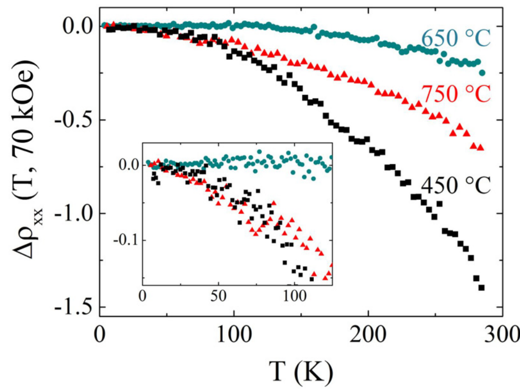

FIG. 5. (Color online) Field induced resistivity variation $\Delta\rho_{xx}(T,70\,\text{kOe})$ as a function of temperature for the CFAS films annealed at different temperatures. The inset shows a zoom of the low temperature region.

which will be available for anomalous one-magnon scattering, which, in terms, points to a T^3 dependence of the resistivity [37].

In the low-temperature region (40 K $< T <$ 100 K), for the 650 °C annealed film, our analysis gives an exponent $\beta = 2$ (see inset of Fig. 4). A rather similar value was obtained for the 750 °C annealed film and a small increase was observed for the lower temperature annealed films, up to 2.13, in the case of the as-deposited one.

In order to further analyze the temperature dependence of the resistivity in the low-temperature region, we have plotted in Fig. 5 the field-induced resistivity variation, defined as

$$\Delta\rho_{xx}(T,H) = 1 - \frac{\rho_{xx}(T,H) - \rho_{xx}(T,0)}{\rho_{xx}(4\ K,H) - \rho_{xx}(4\ K,0)}, \qquad (3)$$

where H is set to our maximum available field of 70 kOe. It has been shown [38] that since the phononic and electron-electron interactions are weakly dependent on the magnetic field, for high enough magnetic fields and for relative high temperatures, the above defined quantity reflects only the spin-flip electronic scattering processes. As seen in Fig. 5, in the case of the 650 °C annealed film, $\Delta\rho_{xx}(T,70\ \text{kOe})$ is temperature independent up to about 125 K. On the contrary, in the case of the 450 °C and 750 °C annealed films $\Delta\rho_{xx}(T,70\ kOe)$ is temperature dependent starting from about 25 K, and shows a stronger temperature dependence in the case of the 450 °C annealed one. This behavior may be explained by taking into account the chemical ordering of the films. As seen in Fig. 1(b), the 450 °C annealed film shows $B2$ ordering while the 750 °C annealed one shows a degraded $L2_1$ ordering and possible $DO3$ disorder. Therefore these films are not expected to have a half-metallic character and they will present states at the Fermi level for the minority spins which will allow the one-magnon scattering. By increasing the temperature, the number of magnons will increase, which will generate an increase of the longitudinal resistivity. The negative value of $\Delta\rho_{xx}(T,70\,\text{kOe})$ indicates a reduction of the electron-magnon scattering with the application of the 70 kOe magnetic field. This is expected since the application of the magnetic field increases the magnon energy and as a result lowers their number. In the case of the 650 °C annealed film, which shows the highest degree of $L2_1$ ordering, one might expect a half-metallic character. For half-metallic materials, the one magnon scattering is forbidden due to the presence of a gap at the Fermi level for the minority spins. Therefore, it is expected that the magnetic field to have an insignificant influence on the longitudinal resistivity. Indeed, this is the case for the 650 °C annealed film, for which $\Delta\rho_{xx}(T,70\,\text{kOe})$ is roughly temperature independent up to about 125 K. Upon increasing the temperature, the finite temperature spin fluctuations may induce minority states at the Fermi level and make possible the electron-magnon scattering. As a result, the application of the magnetic field is expected to influence the longitudinal resistivity and $\Delta\rho_{xx}(T,70\text{ kOe})$ will gain negative values. This is an indication of the half-metallic character of the CFAS film annealed at 650 °C at low temperatures. It is to be mentioned that a somehow similar behavior of the magnetoresitance was observed for high-quality half-metallic Co_2FeSi Heusler alloy single crystals [39].

2. *Low temperatures $T < 40$ K*

In the low-temperatures region ($T <$ 40 K), all the films show similar a resistivity minimum (ρ_{xx0}) measured at $T_{\text{min}} =$ 15–30 K (inset of Fig. 6) and a small upturn in resistivity for lower temperatures. The presence of a resistivity minimum at low temperatures indicates the occurrence of a quantum correction in resistivity. Figure 6 shows a semilogarithmic plot of the resistivity variation with respect to temperature, defined as $\Delta\rho_{xx} = \rho_{xx}(T) - \rho_{xx0}$. The slope of the $\Delta\rho_{xx}$ temperature logarithmic dependence shows a decrease as the annealing temperature is increased. This suggest that the structural disorder, which is higher for lower temperature annealed films [inset of Fig. 1(b)], is responsible for the logarithmic behavior. Moreover, the slope is at a minimum for the 750 °C annealed film, although for this sample the chemical order is lower than in the case of the 650 °C annealed one. This indicates that the structural disorder and not the chemical disorder is the main responsible for the observed resistivity dependence at low temperatures.

There are a number of mechanisms that can be accountable for this type of resistivity dependence, like the weak localization and/or electron-electron interactions in the

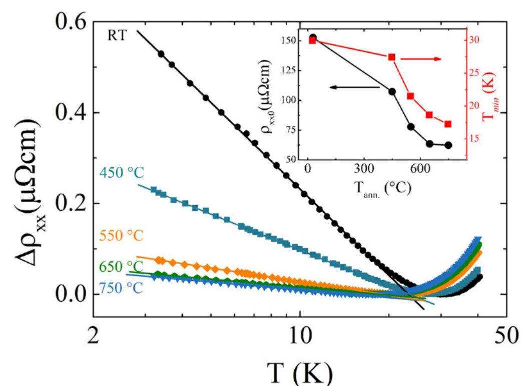

FIG. 6. (Color online) Semilogarithmic plot of the resistivity variation vs temperature for CFAS films annealed at different temperatures. The inset shows the resistivity minimum ρ_{xx0} and the temperature T_{min} at which it was measured. Solid lines show linear fits of $\Delta\rho_{xx}$ vs $\ln T$.

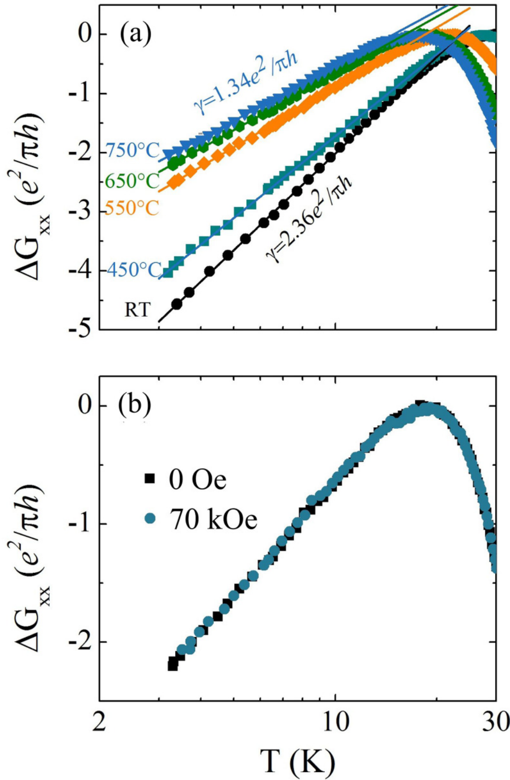

FIG. 7. (Color online) (a) Semilogarithmic plot of the quantum correction to the sheet conductance temperature dependence for the as-deposited and different temperature annealed CFAS films. Solid lines show linear fits of ΔG_{xx} vs $\ln T$. (b) Semilogarithmic plot of the quantum correction to the sheet conductance temperature dependence for the 650 °C annealed film measured in zero and 70 kOe perpendicular applied magnetic field.

presence of disorder [40,41]. For weak localization in the case of two-dimensional systems, for which the thickness of the films is lower than the phase-coherence length L_Φ, the quantum correction to the sheet conductance $\Delta G_{xx} = -\Delta\rho_{xx} d/\rho_{xx}^2$ displays a logarithmic dependence on T. The slope of the quantum correction to the sheet conductance $\gamma = \partial(\Delta G_{xx})/\partial(\ln T)$ gives the dominant inelastic relaxation mechanism and in the case weak localization and/or electron-electron interaction should be of the order of the quantum conductance $L_{00} = e^2/\pi h$, [40,41]. As can be seen in Fig. 7(a), the ΔG_{xx} follows a logarithm T dependence with a slope γ decreasing from $2.36e^2/\pi h$, for the as-deposited film, down to $1.34e^2/\pi h$, for the 750 °C annealed one. These values of the slope could be ascribed to weak localization and/or electron-electron interaction. Since the application of a magnetic field destroys the time reversal symmetry, it is expected that the weak localization and/or electron-electron interactions effects to be suppressed in strong magnetic fields [40,41]. However, our experimental results indicate that the slope of the logarithmic temperature dependence does not change even in magnetic fields as large as 70 kOe [Fig. 7(b)]. This renders the logarithmic temperature dependence of the resistivity difficult to interpret in the context weak localization and/or electron-electron interactions. A rather similar behavior, showing the same logarithmic temperature dependence and magnetic field independence of the low-temperature resistivity variation, was previously reported for magnetically ordered $Mn_5Si_3C_x$ films [42]. It was interpreted in the framework of the orbital Kondo effect derived from two level excitations associated to the structural imperfections located at the grain boundaries, with a Kondo temperature around 1 K. It is tempting to attribute our observed resistivity behavior to the same Kondo effect, however, a precise evaluation of the responsible physical mechanism requires additional analysis of the resistivity down to ultralow millidegree-of-Kelvin temperature range.

C. Hall effect

For a ferromagnetic thin film the transverse Hall resistivity ρ_{xy} was found [43] to follow the empirical relation: $\rho_{xy} = \mathrm{R}_0 H + \mathrm{R}_S 4\pi M_z$, where R_0 and R_S are the ordinary and anomalous Hall constants, H is the applied perpendicular magnetic field, while M_z is the magnetization along the perpendicular to the plane direction. The normal Hall contribution is a consequence of the Lorentz force acting on the conduction electrons and it is usually much smaller than the anomalous one, which is a consequence of the asymmetric carriers diffusion due to the spin-orbit coupling. Figure 8(a) shows a typical Hall effect measurement performed at room temperature on the 650 °C annealed sample. The anomalous Hall contribution is dominant and saturates at a certain saturation field, above which the normal Hall contribution becomes discernible as a linear dependence of ρ_{xy} on the field H. This allows us to extract the anomalous Hall resistivity ρ_{AHE} as the zero-field extrapolation of the high-field $\rho_{xy} = f(H)$ data. Figure 8(b) depicts the temperature dependence of ρ_{AHE} for the CFAS films, which show a decrease with temperature following the same trend as the longitudinal resistivity ρ_{xx}.

Usually, to identify the predominant scattering mechanism responsible for AHE, a simple scaling relation is used: $\rho_{\mathrm{AHE}} = a\rho_{xx} + b\rho_{xx}^2$. Here, the parameter of the linear contribution a stands for the extrinsic skew scattering (SS) of the charge carriers [44]. The parameter of the quadratic dependence b is associated with the extrinsic side jump (SJ) contribution [45] and with intrinsic band structure effects [46], reinterpreted in the light of Berry phase effects on occupied Bloch states [47]. Conventionally, in order to distinguish amongst the different scattering mechanisms, the ρ_{AHE} versus ρ_{xx} data are interpreted using a power-law dependence, i.e., $\rho_{\mathrm{AHE}} \sim \rho_{xx}^{\xi}$. A value of $\xi = 1$ gives a dominant SS mechanism, while $\xi = 2$ indicates a dominant SJ or intrinsic mechanism, respectively. Figure 9 shows the log-log plot of ρ_{AHE} against ρ_{xx} for the CFAS films as deposited and annealed at different temperatures. The exponent ξ is determined by linear fitting the $\ln\rho_{\mathrm{AHE}}$ versus $\ln\rho_{xx}$ data. Interestingly, ξ shows values larger than 2 for all the films, starting with $\xi = 2.4$ for the as deposited sample, up to $\xi = 3.27$ for the 750 °C annealed one. Values of ξ larger than 2 were reported before for heterogenous systems and granular films with enhanced interfacial scattering [48,49]. However, such values are unexpected for homogenous films. This is an indication that the conventional scaling relation is unsuitable for determining the AHE mechanism in our films. Usually, the skew scattering ρ_{sk} contribution to ρ_{AHE} is introduced as linear term $\rho_{sk} = a\rho_{xx}$ [43]. The longitudinal resistivity of the films can be separated into a temperature

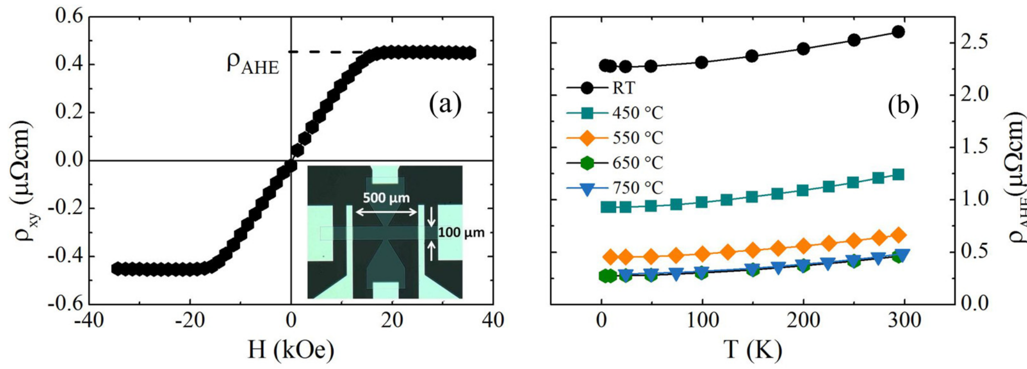

FIG. 8. (Color online) (a) Hall effect measurement performed at room temperature on the 650 °C annealed sample. The inset of shows an optical microscopy image of a Hall patterned element. (b) Temperature dependence of ρ_{AHE} for the CFAS films.

independent ρ_{xx0} and a temperature dependent ρ_{xxT} part as $\rho_{xx}(T) = \rho_{xx0} + \rho_{xxT}(T)$. The temperature independent part is related to scattering on structural imperfections, while the temperature-dependent part is a result of electron-phonon scattering, electron-electron interactions, and electron-spin wave scattering [see Eq. (1)]. It was pointed out theoretically and experimentally that the scattering on structural imperfections could have the dominant contribution on skew scattering [50–52] relative to temperature-dependent contributions. Therefore it is reasonable to ignore all other contributions for skew scattering except the impurity induced one. Furthermore, if the side jump and intrinsic mechanism are introduced as a quadratic dependence, the scaling relation simplifies to $\rho_{\text{AHE}} = a'\rho_{xx0} + b\rho_{xx}^2$, with $a' = \kappa + \lambda\rho_{xx0}$, where κ and λ are two real constants [51–53].

Figure 10 shows ρ_{AHE} plotted against ρ_{xx}^2 for the as deposited film and different temperatures annealed ones. An excellent linear dependence is observed for all the films, in agreement with the new scaling relation $\rho_{\text{AHE}} = a'\rho_{xx0} + b\rho_{xx}^2$. These experimental results seems to point out that, indeed, the impurity induced is the dominant skew scattering contribution for AHE.

Figure 11(a) shows the extracted intrinsic AHE parameter b by fitting the data to the $\rho_{\text{AHE}} = a'\rho_{xx0} + b\rho_{xx}^2$ scaling relation. The intrinsic constant shows, within the error limits, a rather constant value around 117 $\Omega^{-1}\text{cm}^{-1}$ for annealing temperatures up to 450 °C (ρ_{xx0} down to 77.7 $\mu\Omega$ cm). An increase up to around 134 Ω^{-1} cm^{-1} is observed for higher annealing temperatures (lower ρ_{xx0}). This coincides with the appearance of the $L2_1$ ordering [Fig. 1(b)], which is expected to have an influence on the topology of the Fermi surface, thus modifying the intrinsic parameter. The extrinsic parameter a' exhibits a linear dependence on ρ_{xx0}, as shown in Fig. 11(b), thus allowing to derive the κ and λ parameters. The κ parameter is simply the skew scattering constant, whereas λ represents the side jump impurity term [51].

In the case of the 450 °C annealed film (with $B2$ ordering), the absolute magnitudes of the intrinsic and extrinsic contributions to the ρ_{AHE}, measured at the temperature corresponding to ρ_{xx0}, are given by $\rho_{\text{int}} = b\rho_{xx0}^2 = 1.35$ $\mu\Omega$ cm for the intrinsic, $\rho_{sj} = \lambda\rho_{xx0}^2 = 9 \times 10^{-2}$ $\mu\Omega$ cm for the side jump, and $\rho_{sk} = \kappa\rho_{xx0} = -4.7 \times 10^{-1}$ $\mu\Omega$ cm for the skew scattering contribution. Although the intrinsic term is dominating, both the skew scattering and side jump terms cannot be neglected even though the later is more important than the former. The relative magnitude of skew scattering term with

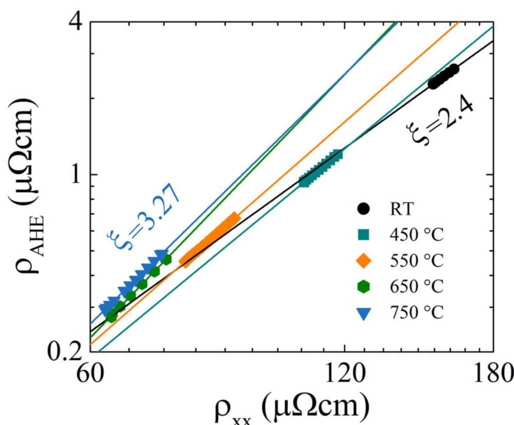

FIG. 9. (Color online) Log-log plot of ρ_{AHE} vs ρ_{xx} for the CFAS films as deposited and annealed at different temperatures. Solid lines show linear fits of ln ρ_{AHE} vs ln ρ_{xx}.

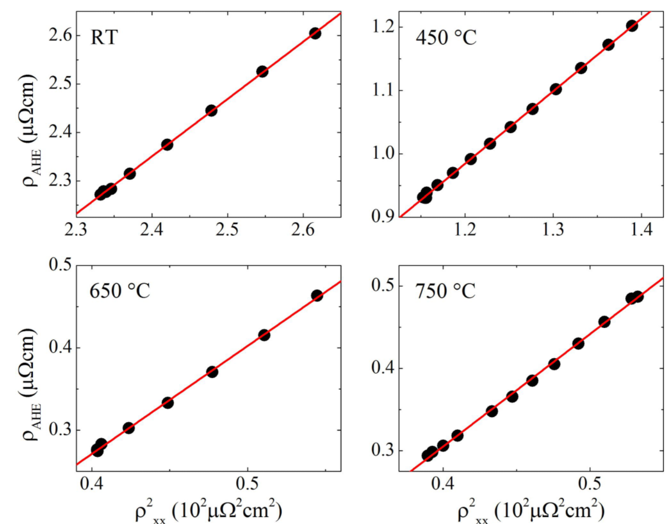

FIG. 10. (Color online) ρ_{AHE} vs ρ_{xx}^2 for the as deposited film and different temperatures annealed ones. The red solid lines represent linear fits of ρ_{AHE} vs ρ_{xx}^2.

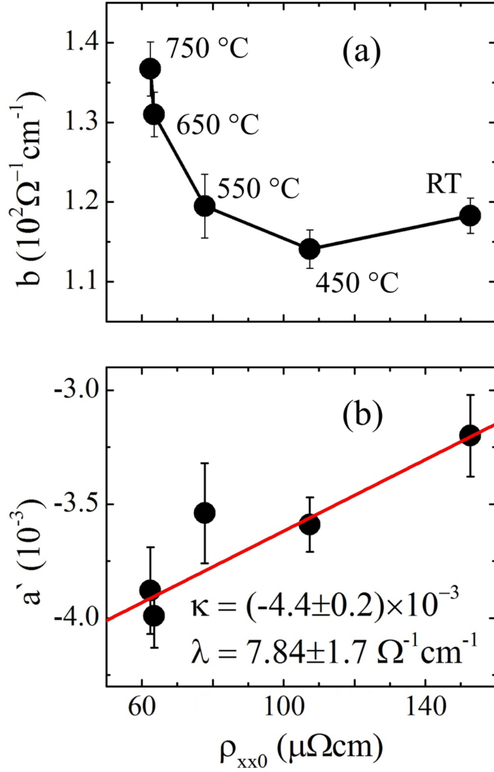

FIG. 11. (Color online) AHE intrinsic (a) and extrinsic (b) parameters with respect to the residual longitudinal resistivity ρ_{xx0}. In (a), the annealing temperatures are indicated. In (b), the red solid line represent a linear fit.

respect to the intrinsic one is given by $|\rho_{sk}|/\rho_{\text{int}} = 0.35$. In the case of the 650 °C annealed film (with $L2_1$ ordering), the absolute magnitudes of the different contributions, are given by: $\rho_{\text{int}} = b\rho_{xx0}^2 = 5.28 \times 10^{-1}$ $\mu\Omega$ cm for the intrinsic, $\rho_{sj} = \lambda\rho_{xx0}^2 = 3.2 \times 10^{-2}$ $\mu\Omega$ cm for the side jump and $\rho_{sk} = \kappa\rho_{xx0} = -2.8 \times 10^{-1}$ $\mu\Omega$ cm for the skew scattering contribution. The intrinsic contribution is still dominant in the case of the 650 °C annealed film with respect to the other contributions. However, the relative magnitude of the skew scattering term with respect to the intrinsic one increases from 0.35 for the $B2$ ordered film up to 0.53 for the $L2_1$ ordered one, respectively. This is a consequence of the important decrease of the ρ_{xx0}, in spite of the increase of the intrinsic b term, for the $B2$ ordered film relative to the $L2_1$ ordered one. Moreover, the negative values of κ indicate that the skew scattering has an opposite contribution to the AHE as compared to the intrinsic or the side jump ones. Therefore, for samples with lower ρ_{xx0} as a function of temperature, the skew scattering may become dominant over the intrinsic contribution and could lead to a change of sign of AHE as the temperature is lowered. This explains the already experimentally observed sign change of AHE with temperature in CFAS films [23].

D. Magnetic properties

For all the studied films, hysteresis loops were measured using a vibrating sample magnetometer with an in-plane magnetic field applied along various orientations ϕ_H (measured relative to one of the substrate edges which coincides with ⟨110⟩ CFAS crystallographic direction). Figure 12 shows representative hysteresis loops recorded for the 650 °C annealed sample. Depending on the field orientation, the loops show different shapes. For $\phi_H = 0°$ a square loop is observed with one step switching, while for $\phi_H = 90°$ two-step magnetization switching is obtained. For $\phi_H = 45°$ and 135°, typical fourfold anisotropy hard axis hysteresis loops are observed. This type of behavior was previously reported for Heusler alloys [5,7,20,30] and qualitatively agrees with a description of the in-plane anisotropy in terms of a superposition of fourfold and twofold contributions. As a consequence, the dynamic magnetic measurements, carried out by broad microstrip line FMR (MS-FMR) technique, were interpreted assuming a magnetic energy density which, in addition to the Zeeman and demagnetizing contributions, contains a perpendicular uniaxial and an in-plane uniaxial and fourfold anisotropy contributions [7]:

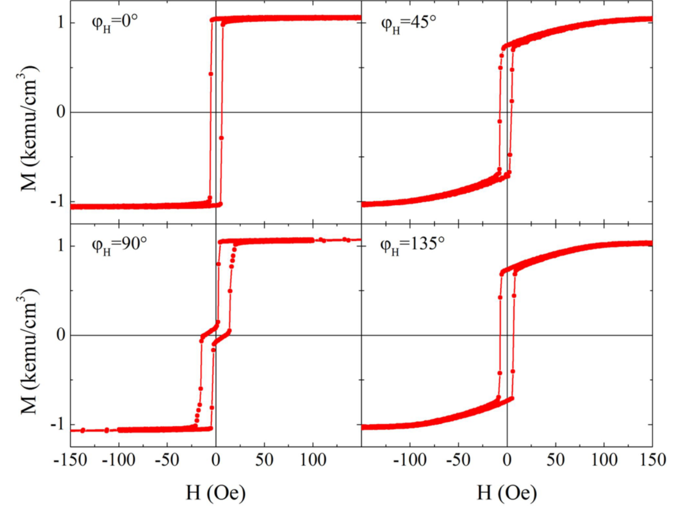

FIG. 12. (Color online) VSM hysteresis loops measured for the 650 °C annealed sample at different in plane field orientation angles ϕ_H.

$$\begin{aligned} E = & -M_s H[\sin\theta_M \sin\theta_H \cos(\phi_M - \phi_H) + \cos\theta_M \cos\theta_H] \\ & - \left(2\pi M_s^2 - K_\perp\right)\sin^2\theta_M - \tfrac{1}{2}K_u[1 + \cos 2(\phi_M - \phi_u)] \\ & \times \sin^2\theta_M - \tfrac{1}{8}K_4[3 + \cos 4(\phi_M - \phi_4)]\sin^4\theta_M, \end{aligned} \quad (4)$$

where θ_M and ϕ_M represent the out-of-plane and the in-plane (relative to one of the substrate edges) angles defining the direction of the magnetization $\mathbf{M}$; ϕ_u and ϕ_4 define the angles between the easy uniaxial planar axis and an easy planar fourfold axis with respect to the substrate edge. K_u, K_4, and $K_\perp$ are the in-plane uniaxial, fourfold and out-of-plane uniaxial anisotropy constants, respectively. As in Ref. [7], we introduce the effective magnetization field $4\pi M_{\text{eff}} = 4\pi M_s - 2K_\perp/M_s = 4\pi M_s - H_\perp$, the uniaxial and the fourfold in-plane anisotropy fields as $H_u = 2K_u/M_s$ and $H_4 = 4K_4/M_s$.

1. *Gyromagnetic factor and effective magnetization*

The MS-FMR technique, in perpendicular configuration, allows deriving the values of the gyromagnetic factor γ and

effective magnetization $4\pi M_{\mathrm{eff}}$ from the variation of the uniform procession modes resonance frequencies versus the magnitude of the perpendicular applied field. The MS-FMR perpendicular field-dependence of the resonance frequencies for all samples is shown in Fig. 13(a). Their linear variations versus the magnetic field is in excellent agreement with the calculated ones using the model presented in Ref. [7] and gives a $\gamma/2\pi = 29.2\,\mathrm{GHz/T}$, independent on the annealing temperature. Figure 13 also indicate that the effective demagnetizing field (effective magnetization) increases with annealing temperature. This effect will be discussed below after presenting the MS-FMR measurements for in-plane applied magnetic fields.

2. *Magnetic anisotropy*

Typical MS-FMR angular dependencies of the uniform precession mode resonance fields at 12 GHz driving frequency of the as-grown and different temperatures annealed CAFS films are shown in Fig. 14(a). The angular behavior of the resonance field is governed by superposition of small uniaxial and a dominating fourfold anisotropies having parallel easy axes: their common axis coincides with one of the substrate edges and, consequently, with one of the ⟨110⟩ type crystallographic directions of the CFAS crystal. The epitaxial symmetry properties of the CFAS films agree with the principal directions of the fourfold contribution suggesting a magnetocrystalline origin of the fourfold anisotropy, while the origin of the uniaxial anisotropy remains unclear. The corresponding field dependence of the frequencies of the uniform precession modes recorded for the applied field along the easy ($\phi_H = 0^\circ$) and hard ($\phi_H = 45^\circ$) axes of CFAS thin films are shown in Fig. 14(b). By fitting the data in Fig. 14 to the above-summarized model (see Ref. [7] for more details), the gyromagnetic factor, the in-plane anisotropy fields and the effective magnetization ($4\pi M_{\mathrm{eff}}$) can be extracted.

The fourfold anisotropy field (H_4) shows a minimal value for the 650 °C annealed sample, for which the $L2_1$ phase is obtained, and increases above this temperature as the $L2_1$ ordering is degraded [as probed by XRD Fig. 1(b)]. Therefore the fourfold anisotropy is correlated to atomic disorder and it is minimal for the perfect chemical ordering, which is in agreement with other reports [5,54]. In contrast,

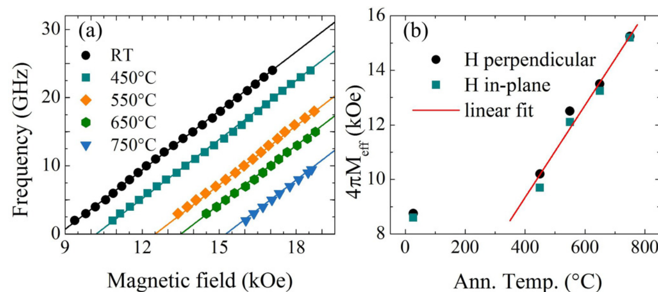

FIG. 13. (Color online) Variation of the (a) frequencies of the uniform precession modes and (b) of the effective magnetization $4\pi M_{\mathrm{eff}}$ for the CFAS films annealed at different temperatures. In (a), the solid lines indicate the fit using the model described in Ref. [7], while in (b), the solid line indicates a linear fit.

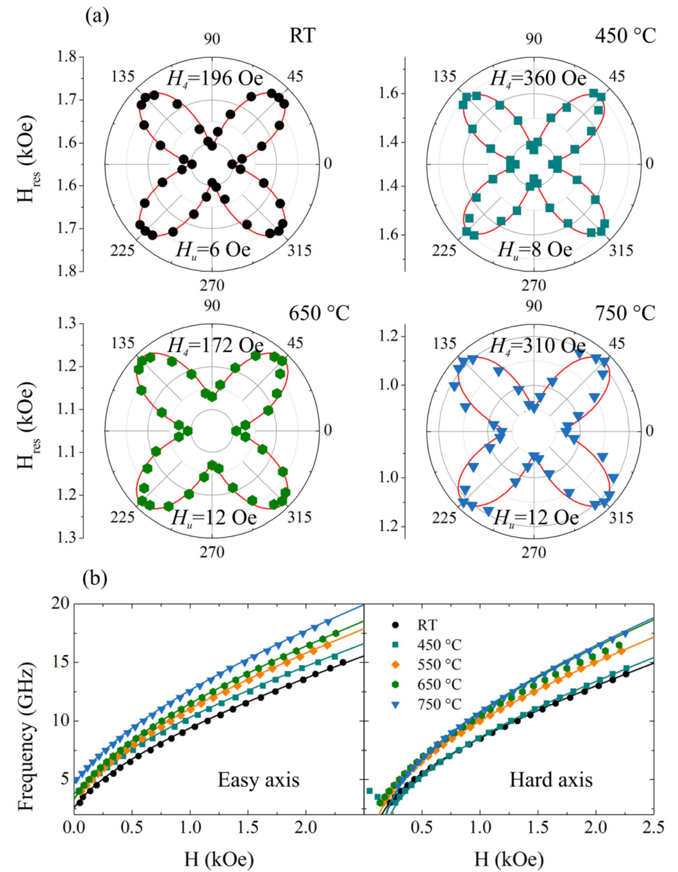

FIG. 14. (Color online) (a) Angular dependence of the resonance field of the uniform precession at 12 GHz for the CFAS films annealed at various temperatures. (b) Field dependence of the resonance frequency of the uniform mode for the CFAS films annealed at various temperatures with the magnetic field applied in the film plane along the easy and the hard magnetic anisotropy axes. The solid lines depicts theoretical fits are obtained using model described in text.

although relative small the observed uniaxial anisotropy field (H_u) shows an increase with annealing temperature up to 12 Oe but remains rather independent on chemical ordering. The extracted effective magnetization from the MS-FMR measurements (for in-plane and perpendicular to the plane applied fields), shown in Fig. 13(b), increases linearly with the annealing temperature in the 450 °C–750 °C range, leading to negative perpendicular anisotropy. This perpendicular magnetic anisotropy derives from a surface energy term which originates from the CFAS/MgO interface whose quality is improving with the annealing temperature. It leads to an enhancement of the effective magnetization that tends to favour the in-plane orientation of the magnetization. Similar behavior has been observed for Co_2FeAl thin films grown on (001) MgO substrates [7].

3. *FMR linewidth*

The in-plane angular and frequency dependencies of the MSFMR spectra have been measured for each sample in order to extract the peak to peak field FMR linewidth (ΔH^{PP}), defined as the separation in field between the extrema of the FMR derivative curves. The frequency dependence of the FMR

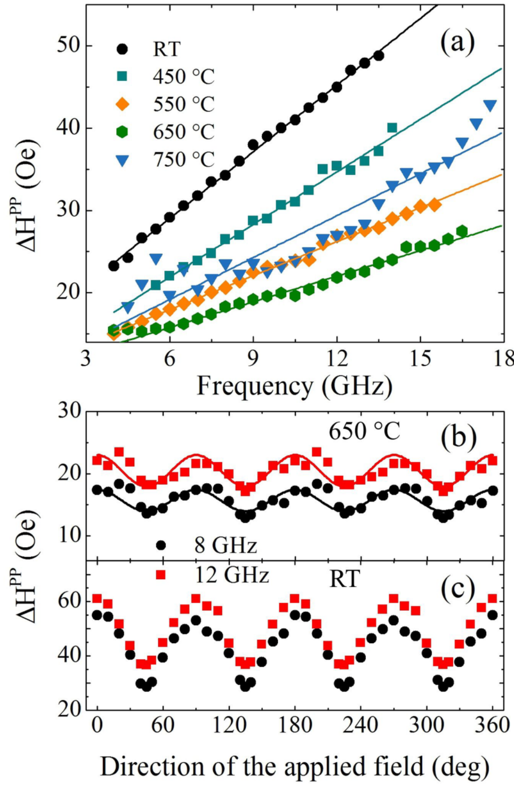

FIG. 15. (Color online) (a) Frequency dependence of the hard axis peak to peak field FMR linewidth (ΔH^{PP}) for CFAS thin films annealed at different temperatures. The solid lines represent linear fits. (b) Angular dependence of the peak to peak field FMR linewidth of the as deposited and the 650 °C annealed films at 8 and 12-GHz driving frequencies. The solid lines for the 650 °C annealed film refer to the fit using the model described in Ref. [7].

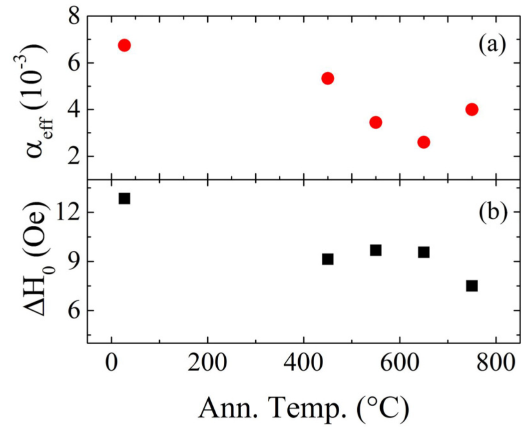

FIG. 16. (Color online) Annealing temperature dependence of the (a) effective Gilbert damping parameter and (b) zero-frequency FMR linewidth for the as deposited and different temperature annealed CFAS films.

linewidth for applied fields parallel to the hard axis for the CFAS films annealed at different temperatures, depicted in Fig. 15(a), shows that the linewidth decreases with increasing the annealing temperature and reaches its minimal values at 650 °C for which the $L2_1$ phase is obtained. Further increasing of the annealing temperature results in the increase of the linewidth due to the degradation of the $L2_1$ ordering. Typical obtained angular dependencies are shown in Figs. 15(b) and 15(c) for the as deposited and 650 °C annealed samples for two driving frequencies of 8 and 12 GHz. It shows a fourfold symmetry (in agreement with the variation of the resonance position) and presents a minimal value for the applied field parallel to the hard axis. Such behavior cannot be attributed to the Gilbert damping contribution, which is expected to be isotropic, and must be connected to additional extrinsic damping mechanisms, such as two magnon scattering. Due to its improved crystalline structure the anisotropy of ΔH^{PP} for the film annealed at 650 °C is lower than that for the as-deposited one. The existence of additional less resolved modes, besides the uniform precession mode, for some applied field directions, due probably to the inhomogeneities (different chemical ordering phases mixture) prevents precise FMR linewidth measurements for the other samples. Therefore our model presented in Ref. [7] cannot be used in analysis the FMR linewidths since this model needs to fit conjointly the angular and frequency dependencies of the linewidth, to determine the intrinsic Gilbert damping parameter and the involved other extrinsic mechanisms. To quantify the effect of the annealing on linewidth in all the samples, only the frequency dependence of the hard axis linewidth, where minimal values are obtained and thus minimal extrinsic contributions to ΔH^{PP} are present, will be analyzed. In a first step, the effective damping Gilbert parameter (α_{eff}) was evaluated using the following expression:

$$\Delta H^{PP} = \frac{2}{\sqrt{3}}\frac{2\pi}{\gamma} \times \alpha_{\mathrm{eff}} f + \Delta H_0, \tag{5}$$

where ΔH_0 describes the linewidth arising from inhomogeneous broadening. The obtained values of the effective (α_{eff}) damping and inhomogeneous broadening ΔH_0 are shown in Fig. 16. The inhomogeneous broadening ΔH_0 shows a decrease as the annealing temperature is increased with a minimum for the 750 °C annealed sample, which shows the best structural properties [inset of Fig. 1(b)]. However, the minimum value of α_{eff} is obtained for the sample annealed at 650 °C sample, which shows the maximum degree of $L2_1$ ordering and which is expected to show a half-metallic character. For the sample annealed at 750 °C, the $L2_1$ ordering is degraded and α_{eff} shows an increase, although this sample shows the best crystal properties. These facts stress the strong correlation between the chemical ordering and damping for Heusler alloys. Based on the band model, the Gilbert damping constant is roughly proportional with the total density of states (DOS) at the Fermi level [6]. Therefore the transition from $B2$ to $L2_1$ chemical ordering which induces a decrease of DOS for minority spins is expected to reduce the damping constant value.

Finally, the observed angular and frequency dependencies of the field linewidth for the film annealed at 650 °C have been analyzed conjointly by considering intrinsic and extrinsic contributions (two magnon scattering), using the similar method described in Ref. [7]. This analysis shows that intrinsic Gilbert coefficient is found to be 1.9×10^{-3}, value which is between the minimal ones obtained for the parent compounds Co_2FeAl

(1×10^{-3}) [7] and Co_2FeSi (2.2×10^{-3}) [9] epitaxial thin films.

IV. CONCLUSIONS

In this paper, we presented a correlated analysis of the structural, longitudinal and transverse electronic transport, and magnetic static and dynamic properties of $Co_2FeAl_{0.5}Si_{0.5}$ Heusler alloy epitaxial thin films grown on MgO(001) single-crystal substrates. The chemical ordering of the films varies form $B2$ to $L2_1$ ordering with respect to the annealing temperature. An optimum annealing temperature is observed, below and above which the $L2_1$ ordering is degraded. Longitudinal magnetoresistivity experiments revealed that for the best $L2_1$ ordered film at temperatures bellow 125 K the magnon assisted electronic scattering is quenched indicating the appearance of half-metallic gap. The presence of a quantum correction in resistivity was evidenced at low temperatures, which manifest itself as logarithmic temperature dependence of the resistivity. Anomalous Hall experiments indicated that the intrinsic band structure contribution is dominant. Moreover, the extrinsic skew scattering contribution is non-negligible and has an opposite sign compared to the intrinsic one. The static and dynamic magnetic characterizations of the CFAS films pointed out to the presence of a small uniaxial magnetic anisotropy contribution superimposed on a larger biaxial. The biaxial term is well correlated with chemical ordering, having a minimum value for the optimum $L2_1$ ordered film. The damping coefficient was evaluated from ferromagnetic resonance linewidth measurements. A Gilbert damping coefficient as low as 1.9×10^{-3} was obtained. The detailed correlated knowledge of the structural, electronic transport and magnetic properties is a prerequisite of the successful integration of $Co_2FeAl_{0.5}Si_{0.5}$ Heusler films in spintronic devices.

ACKNOWLEDGMENTS

This work has been supported by the Exploratory Research Project SPINTAIL: PN-II-ID-PCE-2012-4-0315, No. 23/29.08.2013, by the project SPINTRONIC: POS CCE ID. 574, code SMIS-CSNR 12467, and by TUCN-MADSPIN Research Project.

[1] G. A. Prinz, Science **282**, 1660 (1998).
[2] R. A. de Groot, F. M. Mueller, P. G. van Engen, and K. H. J. Buschow, Phys. Rev. Lett. **50**, 2024 (1983).
[3] I. Galanakis, P. H. Dederichs, and N. Papanikolaou, Phys. Rev. B **66**, 174429 (2002).
[4] S. Picozzi, A. Continenza, and A. J. Freeman, Phys. Rev. B **66**, 094421 (2002).
[5] S. Trudel, G. Wolf, J. Hamrle, B. Hillebrands, P. Klaer, M. Kallmayer, H.-J. Elmers, H. Sukegawa, W. Wang, and K. Inomata, Phys. Rev. B **83**, 104412 (2011).
[6] S. Mizukami, D. Watanabe, M. Oogane, Y. Ando, Y. Miura, M. Shirai, and T. Miyazaki, J. Appl. Phys. **105**, 07D306 (2009).
[7] M. Belmeguenai, H. Tuzcuoglu, M. S. Gabor, T. Petrisor, C. Tiusan, D. Berling, F. Zighem, T. Chauveau, S. M. Chérif, and P. Moch, Phys. Rev. B **87**, 184431 (2013).
[8] M. Oogane, R. Yilgin, M. Shinano, S. Yakata, Y. Sakuraba, Y. Ando, and T. Miyazaki, J. Appl. Phys. **101**, 09J501 (2007).
[9] F. J. Yang, C. Wei, and X. Q. Chen, Appl. Phys. Lett. **102**, 172403 (2013).
[10] W. Wang, H. Sukegawa, R. Shan, S. Mitani, and K. Inomata, Appl. Phys. Lett. **95**, 182502 (2009).
[11] Z. Gercsi, A. Rajanikanth, Y. K. Takahashi, K. Hono, M. Kikuchi, N. Tezuka, and K. Inomata, Appl. Phys. Lett. **89**, 082512 (2006).
[12] D. Ralph and M. Stiles, J. Magn. Magn. Mater. **320**, 1190 (2008).
[13] J. Childress, M. Carey, S. Maat, N. Smith, R. Fontana, D. Druist, K. Carey, J. Katine, N. Robertson, T. Boone, M. Alex, J. Moore, and C. Tsang, IEEE Trans. Magn. **44**, 90 (2008).
[14] G. H. Fecher and C. Felser, J. Phys. D **40**, 1582 (2007).
[15] T. M. Nakatani, T. Furubayashi, S. Kasai, H. Sukegawa, Y. K. Takahashi, S. Mitani, and K. Hono, Appl. Phys. Lett. **96**, 212501 (2010).
[16] H. Sukegawa, S. Kasai, T. Furubayashi, S. Mitani, and K. Inomata, Appl. Phys. Lett. **96**, 042508 (2010).
[17] T. Furubayashi, K. Kodama, H. Sukegawa, Y. K. Takahashi, K. Inomata, and K. Hono, Appl. Phys. Lett. **93**, 122507 (2008).
[18] R. Shan, H. Sukegawa, W. H. Wang, M. Kodzuka, T. Furubayashi, T. Ohkubo, S. Mitani, K. Inomata, and K. Hono, Phys. Rev. Lett. **102**, 246601 (2009).
[19] Y. Miura, K. Nagao, and M. Shirai, Phys. Rev. B **69**, 144413 (2004).
[20] M. S. Gabor, T. Petrisor, C. Tiusan, M. Hehn, and T. Petrisor, Phys. Rev. B **84**, 134413 (2011).
[21] T. M. Nakatani, A. Rajanikanth, Z. Gercsi, Y. K. Takahashi, K. Inomata, and K. Hono, J. Appl. Phys. **102**, 033916 (2007).
[22] P. Webster and K. Ziebeck, in *Alloys and Compounds of d-Elements with Main Group Elements. Part 2*, Landolt-Brnstein - Group III Condensed Matter, Vol. 19c, edited by H. Wijn (Springer, Berlin, Heidelberg, 1988), pp. 75–79.
[23] E. Vilanova Vidal, H. Schneider, and G. Jakob, Phys. Rev. B **83**, 174410 (2011).
[24] B. Peters, A. Alfonsov, C. G. F. Blum, S. J. Hageman, P. M. Woodward, S. Wurmehl, B. Bchner, and F. Y. Yang, Appl. Phys. Lett. **103**, 162404 (2013).
[25] M. Wójcik, E. Jedryka, H. Sukegawa, T. Nakatani, and K. Inomata, Phys. Rev. B **85**, 100401 (2012).
[26] R. Y. Umetsu, A. Okubo, and R. Kainuma, J. Appl. Phys. **111**, 073909 (2012).
[27] A. Alfonsov, B. Peters, F. Y. Yang, B. Büchner, and S. Wurmehl, Phys. Rev. B **91**, 064421 (2015).
[28] M. Obaida, K. Westerholt, and H. Zabel, Phys. Rev. B **84**, 184416 (2011).
[29] M. P. Raphael, B. Ravel, Q. Huang, M. A. Willard, S. F. Cheng, B. N. Das, R. M. Stroud, K. M. Bussmann, J.

H. Claassen, and V. G. Harris, Phys. Rev. B **66**, 104429 (2002).

[30] T. Ambrose, J. J. Krebs, and G. A. Prinz, Appl. Phys. Lett. **76**, 3280 (2000).

[31] H. Schneider, G. Jakob, M. Kallmayer, H. J. Elmers, M. Cinchetti, B. Balke, S. Wurmehl, C. Felser, M. Aeschlimann, and H. Adrian, Phys. Rev. B **74**, 174426 (2006).

[32] M. R. Paudel, C. S. Wolfe, H. Patton, I. Dubenko, N. Ali, J. A. Christodoulides, and S. Stadler, J. Appl. Phys. **105**, 013716 (2009).

[33] D. A. Goodings, Phys. Rev. **132**, 542 (1963).

[34] I. Mannari, Prog. Theor. Phys. **22**, 335 (1959).

[35] T. Kasuya, Prog. Theor. Phys. **22**, 227 (1959).

[36] M. I. Katsnelson, V. Y. Irkhin, L. Chioncel, A. I. Lichtenstein, and R. A. de Groot, Rev. Mod. Phys. **80**, 315 (2008).

[37] N. Furukawa, J. Phys. Soc. Jpn. **69**, 1954 (2000).

[38] B. Raquet, M. Viret, E. Sondergard, O. Cespedes, and R. Mamy, Phys. Rev. B **66**, 024433 (2002).

[39] D. Bombor, C. G. F. Blum, O. Volkonskiy, S. Rodan, S. Wurmehl, C. Hess, and B. Büchner, Phys. Rev. Lett. **110**, 066601 (2013).

[40] G. Bergmann, Phys. Rep. **107**, 1 (1984).

[41] P. Lee and T. Ramakrishnan, Rev. Mod. Phys. **57**, 287 (1985).

[42] B. Gopalakrishnan, C. Sürgers, R. Montbrun, A. Singh, M. Uhlarz, and H. Löhneysen, Phys. Rev. B **77**, 104414 (2008).

[43] N. Nagaosa, J. Sinova, S. Onoda, A. H. MacDonald, and N. P. Ong, Rev. Mod. Phys. **82**, 1539 (2010).

[44] J. Smit, Physica **24**, 39 (1958).

[45] L. Berger, Phys. Rev. B **2**, 4559 (1970).

[46] R. Karplus and J. M. Luttinger, Phys. Rev. **95**, 1154 (1954).

[47] D. Xiao, M.-C. Chang, and Q. Niu, Rev. Mod. Phys. **82**, 1959 (2010).

[48] S. N. Song, C. Sellers, and J. B. Ketterson, Appl. Phys. Lett. **59**, 479 (1991).

[49] P. Xiong, G. Xiao, J. Q. Wang, J. Q. Xiao, J. S. Jiang, and C. L. Chien, Phys. Rev. Lett. **69**, 3220 (1992).

[50] A. Crépieux and P. Bruno, Phys. Rev. B **64**, 014416 (2001).

[51] Y. Tian, L. Ye, and X. Jin, Phys. Rev. Lett. **103**, 087206 (2009).

[52] L. Ye, Y. Tian, X. Jin, and D. Xiao, Phys. Rev. B **85**, 220403 (2012).

[53] D. Hou, Y. Li, D. Wei, D. Tian, L. Wu, and X. Jin, J. Phys. Condens. Matter **24**, 482001 (2012).

[54] S. Trudel, O. Gaier, J. Hamrle, and B. Hillebrands, J. Phys. D **43**, 193001 (2010).